Oxygen mobility in the perovskite $SrTi_{1-x}Fe_xO_{3-\delta}$ ($x=0.8$)

E. Mashkina and A. Magerl
Lehrstuhl für Kristallographie und Strukturphysik, Universität Erlangen-Nürnberg, 91058 Erlangen, Germany

J. Ollivier
Institut Laue-Langevin, 6 rue Jules Horowitz, BP 156, 38042 Grenoble, France

M. Göbbels
Lehrstuhl für Mineralogie, Universität Erlangen-Nürnberg, 91054 Erlangen, Germany

F. Seifert
Bayerisches Geoinstitut, Universität Bayreuth, 95440 Bayreuth, Germany

(Received 30 March 2006; revised manuscript received 24 August 2006; published 12 December 2006)

The dynamics of long range translation and local motions of oxygen in $SrTi_{0.2}Fe_{0.8}O_{3-\delta}$ have been studied by electrical conductivity and quasielastic neutron scattering. The activation energy of the translational ionic diffusion measured by electrical conductivity is 0.97 eV for $T>900$ °C. Both quasielastic linewidths and quasielastic intensities in neutron scattering show the presence of two motions. The Q independences indicate a localized character for these oxygen diffusion modes with activation energies of 0.43 and 0.27 eV for the "fast" and the "slow" local jumps, respectively. A model for the local oxygen motion is proposed involving oxygen jumps in the (0 k 0) plane either directly to the next unit cell or performing detours combining two and two site jumps resulting in the same final momentum transfer.

DOI: 10.1103/PhysRevB.74.214106 PACS number(s): 61.12.Ex, 61.72.Ji, 66.30.Dn, 66.10.Ed

I. INTRODUCTION

Perovskites of type ABO_3 with A and B representing valence 2+ and 4+ cations can be made mixed ionic-electronic conducting by doping on the B site with trivalent ions at a concentration level of several mol %. Such materials exhibit interesting transport properties as well as good thermodynamic stability over a large range of temperature and oxygen partial pressure. They have a strong potential for applications in high temperature electrochemical devices including oxygen separation membranes and solid oxide fuel cells. A further development and optimization of oxide conductors suitable for use at lower temperatures calls for an understanding of the mechanisms by which the anions move in the solid. This includes a determination of the oxygen sites that contribute to conductivity and those that remain permanently occupied in the solid. However, a characterization of the particle dynamics in fast ionic conductors is a formidable task since there is a large number of interacting charged particles in a disordered environment.

The system $SrTi_{1-x}Fe_xO_{3-\delta}$ was synthesized by Clevenger[1] who interpreted the electronic properties in terms of an electron-hopping mechanism occurring between Fe^{3+}-Fe^{4+} pairs. In a further study Brixner[2] synthesized samples in a reducing atmosphere. He came to the same conclusions as Clevenger concerning conductivity of the perovskite samples. However, up to now there is no accepted explanation for the spatial distribution of the oxygen vacancies in this system.

The phase diagram of the $SrTi_{1-x}Fe_xO_{3-\delta}$ system is not well established and the published data are inconsistent. According to Ref. 3 the transition of the end member $Sr_2Fe_2O_5$ from the low temperature ordered form (brownmillerite structure) to the high temperature disordered form (perovskite structure) observed at about 850 °C was explained by the formation of microdomains. At intermediate concentrations such as $SrTi_{1-x}Fe_xO_{3-\delta}$ with $x=0.8$ superstructures relating to a two-dimensional (2D) ordering of vacancies builds up as identified by high resolution transmission electron microscopy (TEM).[4] Steinsvik *et al.*[5] investigated the defect ordering in the composition range $0\leq x\leq 0.8$ by TEM and electron diffraction. For $x<0.5$ only the cubic perovskite structure was found. However, ordering of oxygen vacancies was observed for samples with $x=0.6$ and $x=0.8$ quenched from 1000 °C in oxidizing and reducing atmospheres. In contrast, Rodriguez[6] did not observe any superstructure lines using x-ray and electron diffraction. Also, electron microscopy did not provide any evidence for oxygen vacancy ordering. These results indicate that: (a) The anionic vacancies

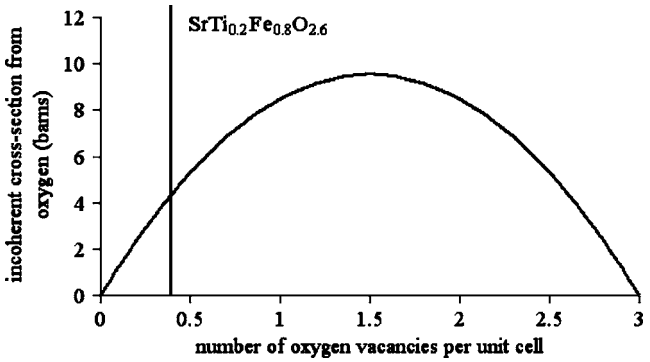

FIG. 1. Concentration dependence of the incoherent cross section from oxygen defects according to Eq. (4). The vertical line indicates the composition of interest.

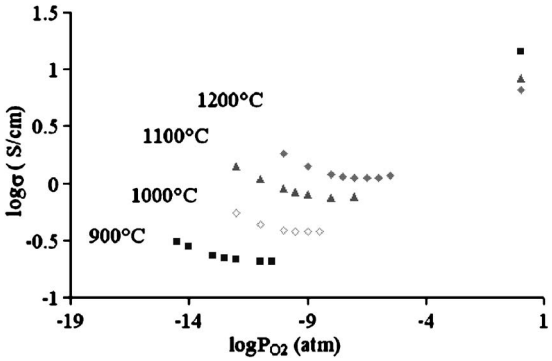

FIG. 2. Total electrical conductivity for $SrTi_{0.2}Fe_{0.8}O_{3-\delta}$ measured at different temperatures.

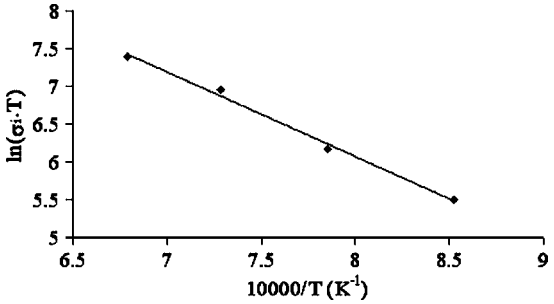

FIG. 3. Arrhenius plots for the ionic conductivity for $SrTi_{0.2}Fe_{0.8}O_{3-\delta}$.

are either randomly distributed or (b) in the case of ordering, it would not be periodic and its contribution to the diffraction patterns may only appear as a weak and hardly structured background between Bragg reflections. Moreover, the data in Ref. 5 show an increase of the conductivity values with iron content $0 \leq x \leq 0.8$ as predicted from a simple defect model in which the oxygen vacancy charges compensate for the substitution of titanium by iron.

In this contribution, we present a quasielastic neutron scattering study of $SrTi_{0.2}Fe_{0.8}O_{3-\delta}$ attempting to identify the diffusive oxygen motions on an atomic scale. Two Lorentzian components are discovered which are attributed to confined motions. A comparison with model calculations for the oxygen local diffusion provides a comprehensive description of the local migration of the oxygen defects. These findings are further discussed together with measurements of the electrical conductivity, where the temperature range of 900–1200 °C and oxygen pressures varying from $10^{-5.5}$ to $10^{-14.5}$ atm were used to separate the different contributions to the conductivity and to identify the dominant parameters for the long distance transport of oxygen ions.

II. THEORY

Quasielastic neutron scattering describes an energy broadening of the scattered beam caused by nonperiodic, i.e., diffusive motions. The broadening measured as a function of momentum transfer $\hbar Q$ identifies uniquely the character of the diffusion.

A particular problem when looking for the diffusion dynamics of oxygen is the small incoherent scattering cross section from oxygen. However, the introduction of defects into the oxygen lattice induces significant Laue scattering which can be treated as a single particle incoherent scattering under the condition of a statistical distribution of oxygen vacancies. Although oxygen is tabulated as a practically pure coherent scatterer,[8] the defect nature of the oxygen lattice transforms part of this scattering out of the Bragg peaks into a diffuse intensity with a specific energy characteristic that represents the single particle diffusion. The cross sections for the scattering from oxygen can be calculated according to the following considerations.

Neglecting absorption, the total scattering cross section which describes the neutron-target interaction is $\sigma_{\text{total}} = 4\pi b^2$, where the scattering length b is different for individual isotopes if they exist. Usually, isotopes are randomly distributed which introduces disorder scattering, also called incoherent scattering (actually, spin disorder is another cause of incoherent scattering, which we need not consider further in this context). In the case of two isotopes with scattering lengths b_1 and b_2 and with concentrations c_1 and c_2 with $c_1 + c_2 = 1$, the cross sections for total scattering σ_{total}, coherent scattering σ_{coh}, and incoherent scattering σ_{inc} are[9–11]

$$\sigma_{\text{total}} = 4\pi\langle b^2\rangle = 4\pi(c_1 b_1^2 + c_2 b_2^2), \tag{1}$$

$$\sigma_{\text{coh}} = 4\pi b_{\text{coh}}^2 = 4\pi(c_1 b_1 + c_2 b_2)^2, \tag{2}$$

$$\sigma_{\text{inc}} = \sigma_{\text{total}} - \sigma_{\text{coh}} = 4\pi c_1 c_2 (b_1 - b_2)^2. \tag{3}$$

We now assume that the oxygen lattice of our sample is occupied randomly by two different isotopes, one with the (coherent) scattering length of oxygen b_1 (occupied site) and the other with a scattering length $b_2 = 0$ (oxygen defect). Modifying Eq. (3), we obtain

$$\sigma_{\text{inc}} = \sigma_{\text{total}} - \sigma_{\text{coh}} = 4\pi c_1 (1 - c_1)(b_1 - b_2)^2. \tag{4}$$

The term $c(1-c)$ determines the shape of the incoherent cross section as a function of the concentration of the oxygen inventory (Fig. 1).

This model is used to calculate the individual scattering cross sections in absolute values. The incoherent component, which may become quasielastically broadened due to oxygen mobility, is shown in Fig. 1 and given in column 4 of Table I for our sample composition. We note that it varies with

TABLE I. Calculated cross sections for $SrTi_{0.2}Fe_{0.8}O_{2.6}$.

Composition	σ_{coh} (b)	$\sigma_{\text{inc}}^{\text{metals}}$ (b)	$\sigma_{\text{inc}}^{\text{defects}}$ (b)	σ_{abs} (b)[a]	$\sigma_{\text{inc}}^{\text{metals}}/\sigma_{\text{inc}}^{\text{defects}}$ (%)
0.8	40.9	8.6	4.41	15.9	51.2

[a]The absorption cross section was calculated for the neutron energy $E = 2.08$ meV.

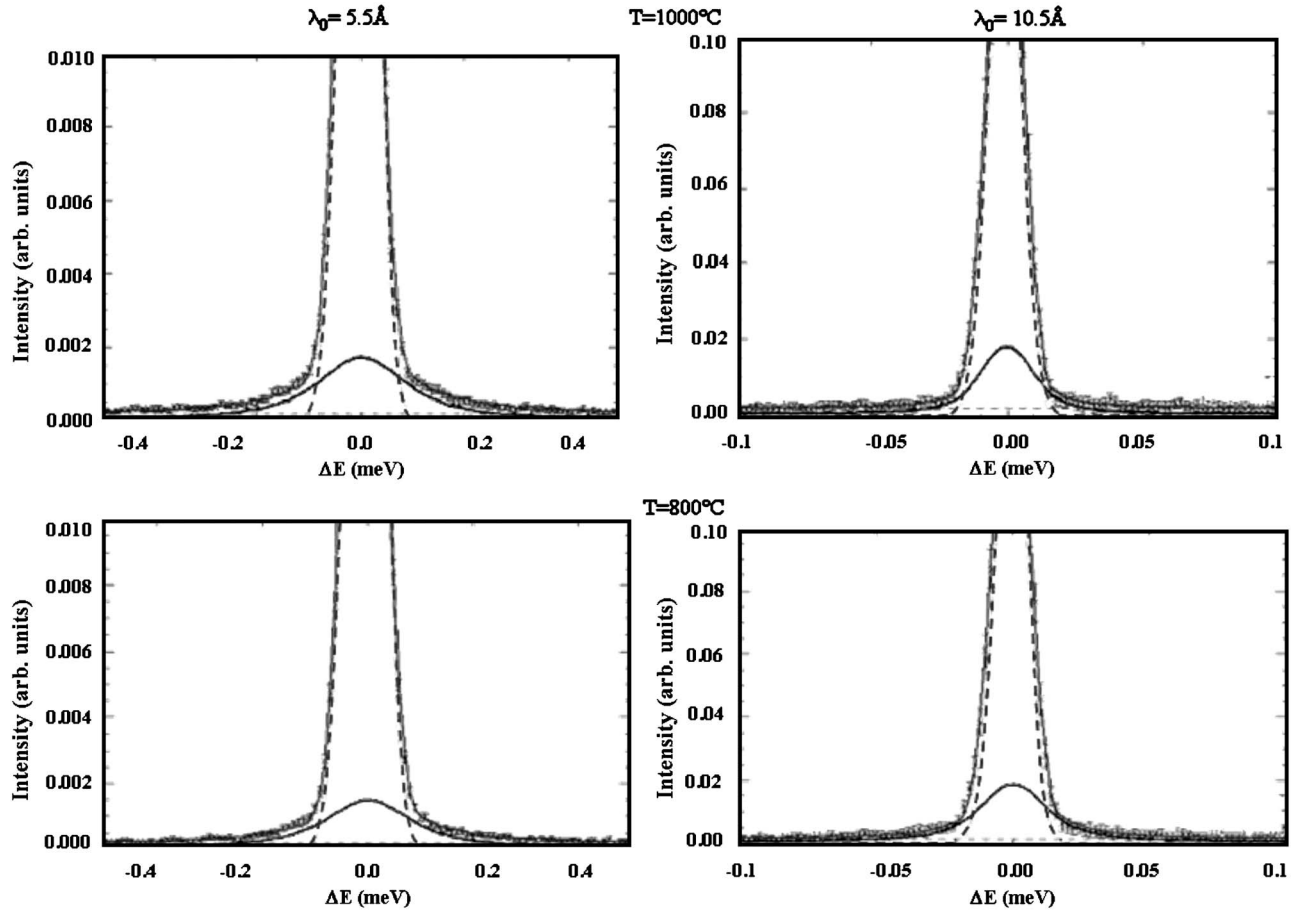

FIG. 4. Examples of quasielastic spectra measured at $Q=0.86$ Å^{-1} at different temperatures and incident wavelengths of 5.5 Å (left panels) and 10.5 Å (right panels). Dark dashed line—resolution function; thick solid line—quasielastic component; gray dashed line—background; thin solid line—resulting fit. Note different ranges for the abscissa on the left and right panels.

composition, but it remains a relatively small contribution under all conditions. This stems largely from the fact that titanium has a high incoherent cross section of 2.67 b.

The classical model for random walk diffusion on Bravais lattices via neighbor sites was derived by Chudley and Elliott.[12] They predicted a single Lorentzian for the incoherent dynamic structure factor $S_{\text{inc}}(Q,\omega)$. In this case the linewidth [full width at half maximum (FWHM)] of the Lorentzian is

$$\Gamma(Q) = \frac{1}{\tau}\left(1 - \frac{\sin(Ql)}{Ql}\right), \tag{5}$$

where τ and l are the mean residence time for the oxygen ions on a lattice site and the length of the jump vector, respectively. For small Q values the sine function can be expanded, resulting in a Q^2 law.

Conductivity in a material may be a more complex phenomenon involving the superposition of different types of motions like a local dynamics which does not contribute to long distance mass transport. Such motions are not detectable by electrical conductivity. The particle stays within a defined volume and the self-correlation function retains a finite component at its place of origin up to infinite times which is expressed in a diffraction experiment by an elastic scattering contribution. In this case, the FWHM of the Lorentzian component is independent of the scattering vector Q as described in Refs. 10–16.

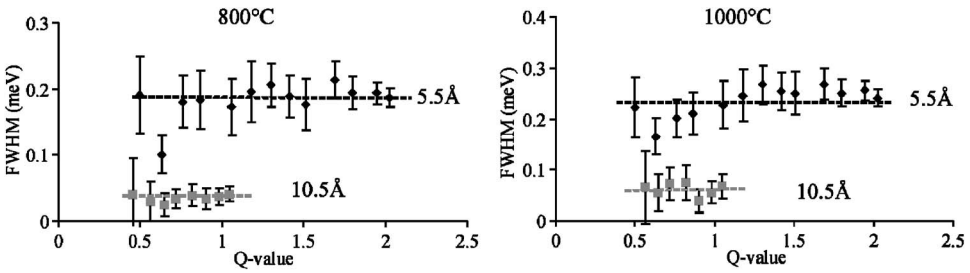

FIG. 5. The Q dependence of the quasielastic linewidths for both resolutions measured at 800 °C and 1000 °C. The FWHMs are independent of the Q value.

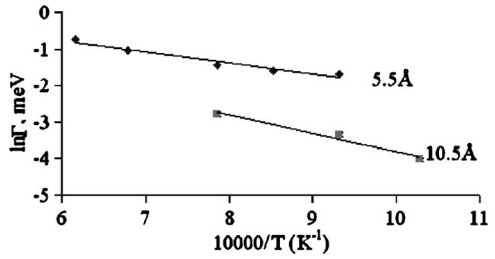

FIG. 6. Arrhenius plot for the quasielastic linewidths measured with incident wavelengths of 5.5 and 10.5 Å.

III. EXPERIMENT

A. Synthesis

Synthesis of $SrTi_{0.2}Fe_{0.8}O_{3-\delta}$ perovskite followed a usual solid state routine. The reagents $SrCO_3$, Fe_2O_3, and TiO_2 powders were dried, appropriately weighed, and mixed under ethanol. A composition was calcinated at $T=1000$ °C for 24 h, then synthesized at a temperature of $T=1200$ °C for 72 h in air with intermediate grinding and x-ray examination. The prepared compound was further analyzed by electron microprobe and x-ray diffraction. The final product reveals a single phase of cubic crystal structure [$a=3.885(2)$ Å] with space group $Pm3m$. Electron microprobe analysis showed that the distribution of the iron was homogeneous and the material was close to the nominal composition [mole fraction of $SrFeO_{2.5}=0.79(1)$].

B. Conductivity measurement

For electrical conductivity measurements, a sample with a rectangular shape ($4.3\times1.5\times14.1$ mm) was used. Four electrodes were deposited by using Pt paste, and Pt wires were attached as current and voltage leads. The accuracy of the oxygen fugacity (H_2/CO_2 gas mixture) is 1 to 5% (depending on the gas ratio). Temperature fluctuations are controlled within ±0.5 °C; the resolution of the electronic characteristics are 1 μV and 1 pA. The measurements were carried out in isothermal runs in the mode of decreasing oxygen partial pressure. Individual data points were recorded by automated equipment upon achievement of equilibrium between the sample and ambient atmosphere.

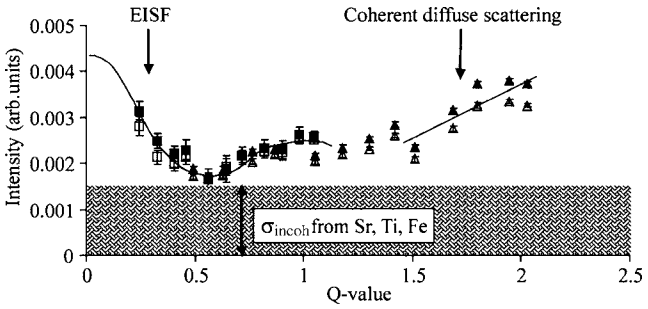

FIG. 7. Elastic incoherent intensity measured at 1000 °C [open squares (10.5 Å); open triangles (5.5 Å)] and at 800 °C [closed squares (10.5 Å); closed triangles (5.5 Å)].

TABLE II. Instrument settings and experimental conditions for the neutron experiment. λ_0 is the wavelength of the incident neutrons, ΔE is the full width at half maximum of the resolution function, and Q is the momentum transfer for elastic scattering.

λ_0(Å)/ΔE (μeV)	Q (Å^{-1})	T (°C)
5.5 Å 70 μeV	$0.45<Q<2.03$	800, 900, 1000, 1200, and 1350
10.5 Å 15 μeV	$0.24<Q<1.05$	700, 800, and 1000

C. Quasielastic neutron scattering

The sample for the quasielastic neutron scattering experiment was heated for periods of 140 h in open AgPd capsules at temperatures of 1200 °C in CO/CO_2 gas mixtures corresponding to an oxygen fugacity of $\ln P_{O2}=-11$. Under these conditions, all iron in the samples is present as Fe^{3+}. Samples were drop quenched into the cool part of the furnace under flowing gas and examined again by x-ray diffraction and Mössbauer spectroscopy to prove the single phase and trivalent iron content.

Quasielastic experiments were performed on the IN5 chopper spectrometer at the ILL, mainly using incident wavelengths of 5.5 and 10.5 Å with resolution widths of the elastic peak of 70 and 15 μeV, respectively (Table II). The use of the two instrumental settings allows a study of the quasielastic broadening due to the oxygen diffusion in a wider dynamic response and in an extended Q range.

The compact powder sample was contained in a thin-walled platinum container (low absorption coefficient) of cylindrical shape to reduce multiple scattering. The raw data were intensity calibrated by a run with a plate of the incoherent scatterer vanadium. The experimental background was measured with the empty Pt container at room temperature. The background includes the contribution in the raw sample data from the furnace and the sample container. Both were subtracted from the raw data. The detectors were grouped for improved counting statistics. Q ranges exhibiting Bragg peaks known from diffraction were excluded from further analysis.

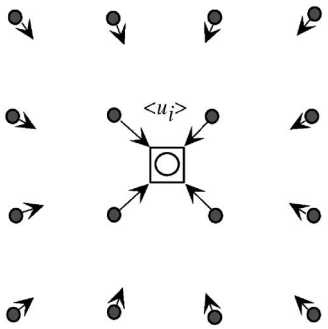

FIG. 8. Displacement field around an oxygen vacancy which is bigger than the transition metal ions and leads to inward shifts u_i.

IV. RESULTS

A. Electrical conductivity

The electrical conductivity σ of $SrTi_{0.2}Fe_{0.8}O_{3-\delta}$ was measured over a broad range of oxygen activities P_{O2} and temperatures (Fig. 2). In the low P_{O2} region, the curves of $\ln \sigma$ show a $-1/4$ slope, attributed to n-type conductivity. At intermediate P_{O2}, the conductivity curves show the beginning of the flat region. This is assigned to an ionic conductivity contribution due to oxygen vacancies, expected independent of P_{O2}. These results and those of others[5,7] are in a good correspondence. The ionic conductivity σ_i in the temperature range of $900\ ^\circ C < T < 1200\ ^\circ C$ is plotted in Fig. 3 as a function of the reciprocal temperature. A linear dependence of $\ln(\sigma_i \cdot T)$ on the reciprocal temperature is observed indicating no structural phase transitions due to ordering of oxygen vacancies. The activation energy E_{act} extracted from the slope of the curve is 0.97 ± 0.01 eV.

B. Quasielastic neutron scattering

1. Quasielastic linewidth

All samples show the presence of quasielastic broadening. Some low-resolution data (i.e., shorter wavelength) are influenced by Bragg scattering at high Q. They were removed from the data set. Data were fitted with a sum of δ function (elastic scattering contributions) and a single Lorentzian (representing the quasielastic scattering from oxygen), both convoluted with the resolution function. In addition, a constant contribution for background was allowed. Figure 4 shows examples of corrected spectra at 1000 °C and 800 °C for both incident wavelengths.

The fast and the slow diffusion components are dominantly visible under the two resolution conditions chosen. The Lorentzian linewidths for both resolutions and at all temperatures do not depend on Q, indicating the localized character of the observed motion (Fig. 5). The following discussion will concentrate on these two motions measured at 800 °C and 1000 °C.

Both quasielastic linewidths increase with temperature, and plotting them logarithmically against the inverse temperature shows their thermally activated character with activation energies of 0.43 ± 0.06 eV and 0.27 ± 0.02 eV for the slower and the faster motion, respectively (Fig. 6).

2. Elastic incoherent structure factor

The characteristic features of the neutron scattering results confirm that the monitored diffusion is a local motion. Decisions between alternative models can be made based on the Q dependence of the elastic incoherent structure factor (EISF). The EISF is the fraction of the total incoherent intensity from the defected oxygen sublattice which is contained in the elastic peak.

Experimental results are shown in Fig. 7 for two measured temperatures: 800 °C and 1000 °C. The data give no indication for a change of the intensities with temperature for $Q < 1.2$ Å^{-1}, indicating that the mechanism of the underlying motion does not change.

Elastic incoherent data show a complex behavior because the sample has an intrinsically high elastic background from Sr, Ti, and Fe. Their contributions add up to the calculated value of 51.2% shown in Table I and Fig. 7. In addition, diffuse elastic scattering becomes dominant at high Q.

3. Short range diffuse scattering

At high Q values, the intensity of the elastic contribution rises monotonically with Q indicating a coherent diffuse contribution (Fig. 7). In the following, a possible interpretation of the coherent quasielastic contribution is given. However, no quantitative analysis is presented because the coherent scattering is outside the topic of the study.

We argue that the coherent contribution observed at higher Q values originates from a relaxation of the host lat-

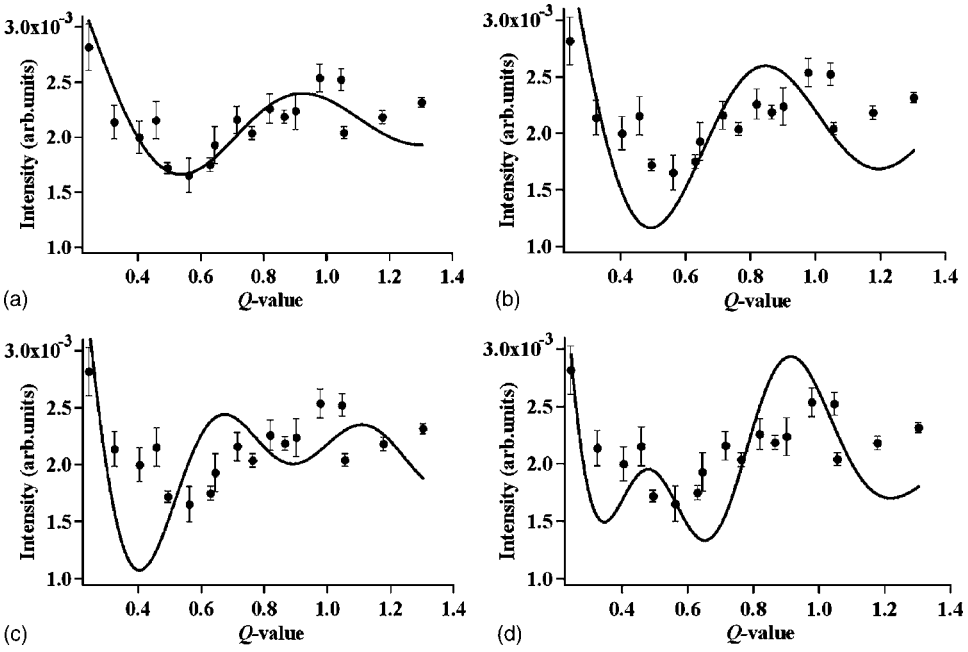

FIG. 9. Elastic incoherent structure factors measured at 1000 °C with wavelengths of 5.5 and 10.5 Å compared to the local motion models of (a) two, (b) three, (c) four, and (d) six sites presented in the text and in Table III.

TABLE III. Expressions for the elastic $A_0(Q)$ and quasielastic $A_1(Q)$ structure factors for the rotational jump models involving two, three, four, and six sites.

$N=2$	$N=3$	$N=4$	$N=6$
$A_0(Q)=\frac{1}{2}[1+j_0(2Qa)]$	$A_0(Q)=\frac{1}{3}[1+2j_0(Qa\sqrt{3})]$	$A_0(Q)=\frac{1}{4}\begin{bmatrix}1+2j_0(Qa\sqrt{2})\\+j_0(2Qa)\end{bmatrix}$	$A_0(Q)=\frac{1}{6}\begin{bmatrix}1+2j_0(Qa)\\+2j_0(Qa\sqrt{3})+j_0(2Qa)\end{bmatrix}$
		$A_1(Q)=\frac{1}{2}[1-j_0(2Qa)]$	$A_1(Q)=\frac{1}{6}\begin{bmatrix}2+2j_0(Qa)\\-2j_0(Qa\sqrt{3})-2j_0(2Qa)\end{bmatrix}$
$A_1(Q)=\frac{1}{2}[1-j_0(2Qa)]$	$A_1(Q)=\frac{2}{3}[1-j_0(Qa\sqrt{3})]$		$A_2(Q)=\frac{1}{6}\begin{bmatrix}2-2j_0(Qa)\\-2j_0(Qa\sqrt{3})+2j_0(2Qa)\end{bmatrix}$
		$A_2(Q)=\frac{1}{4}\begin{bmatrix}1-2j_0(Qa\sqrt{2})\\+j_0(2Qa)\end{bmatrix}$	$A_3(Q)=\frac{1}{6}\begin{bmatrix}1-2j_0(Qa)\\+2j_0(Qa\sqrt{3})-j_0(2Qa)\end{bmatrix}$

tice surrounding a lattice defect (vacancy in our case) (Fig. 8). As was shown in Ref. 17 the Fe^{3+} ions move by about 0.2 Å towards the oxygen vacancy, a value which is much larger than generally assumed for the thermal Debye-Waller factor. The scattering from defects is therefore determined by the interference between contributions of the vacancy itself and the displacement field, where the latter scattering originates from the difference between the deformed and undeformed lattice. If we put an oxygen vacancy at the origin such that the moduli of R_i are the distances between the oxygen vacancy and the undisplaced iron or titanium position, then u_i describes the static displacements of the Fe or Ti atoms. The structure factor due to distortion around the oxygen vacancy is to a first order approximation

$$S(Q)_{\mathrm{dis}} = |1 + e^{iQ\langle u_i\rangle}|^2. \tag{6}$$

This scattering function $S(Q)_{\mathrm{dis}}$ yields diffuse intensities increasing proportionally Q^2 as long as $Q\langle u_i\rangle \ll 2\pi$, which is the condition of our measurements. If the defect is mobile, the scattering develops an elastic and a quasielastic component.[18–20] Note that, at the same time, in Fig. 7, we observe a pronounced thermal Debye-Waller factor leading to reduction of the diffuse coherent contribution at high Q values with temperature.

V. DISCUSSION AND SUMMARY

The common tendency of the EISF to change up to Q values <1.2 Å^{-1} demonstrates a similar character for the two local motions identified (Fig. 7). Because of the incoherent character of the scattering, we consider correlations only between oxygen sites that are visited during the local motion of a vacancy, while assuming that correlations to all other atoms can be neglected. By assuming a model of a local motion between two, three, four, and six energetically equivalent sites, one can calculate the corresponding EISFs and the quasielastic structure factors (Table III). Derivation of theoretical equations is given elsewhere.[9–14]

As an example, Fig. 9 shows a comparison between calculations for the above models and the experimental EISF measured with two incident wavelengths at 1000 °C. The data were fitted up to $Q<1.4$ Å^{-1} excluding the region of coherent scattering at larger momentum transfer. The best fit to the data at 1000 °C is observed for the two sites model with a jump distance of 7.76 ± 0.43 Å. This distance corresponds within the error bars to two times the unit cell parameter for $SrTi_{0.2}Fe_{0.8}O_{3-\delta}$ ($a=3.885$ Å).

Careful analysis of the quasielastic structure factors (Fig. 10) reveals consistently higher intensities for the high resolution data. This shows that there are more crystallographic sites involved in the slower local motion as compared to the faster one. However, within the accuracy of the data the wave vector transfer with maximum quasielastic intensity of 0.82 Å^{-1} remains the same. Thus both the quasielastic linewidths and the quasielastic intensities show the presence of two local modes.

Based on these findings we state that two different types of local motions are observed in the high and low resolution measurements.

As a matter of fact, neutron data were taken at more instrumental settings and at different spectrometers yielding 150, 60, 30, and 1 μeV resolution functions, respectively, without finding further types of local motions. The data pre-

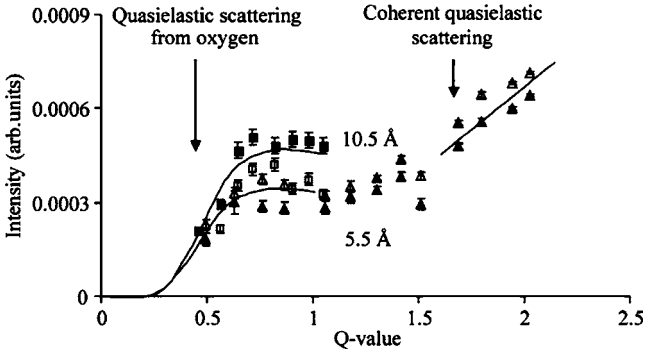

FIG. 10. Measured quasielastic structure factors at 1000 °C [open squares (10.5 Å); open triangles (5.5 Å)] and at 800 °C [closed squares (10.5 Å); closed triangles (5.5 Å)]. Solid lines are a guide to the eye representing the average intensity measured at the same resolution function.

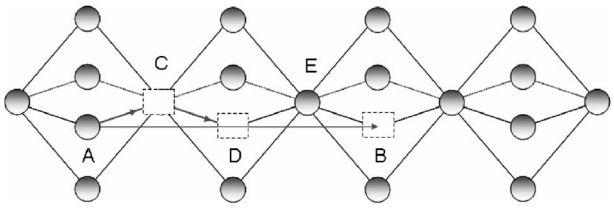

FIG. 11. Two site jump models: Oxygen can perform direct jumps from *A* to *B* (fast motion) or indirect jumps *A*–*C* and *D*–*B* (slow motion).

sented at 5.5 and 10.5 Å on IN5 just show these two types of local motion most clearly.

Following the well known mechanism, Ti^{4+} on octahedral sites is replaced by Fe^{3+} forming oxygen vacancies to balance the charge. As proposed in Refs. 21–23, two Fe atoms form a monomer (a single oxygen vacancy) neighbored by two pentacoordinated sites Fe^{3+}(V). A vacancy dimer is then formed with the substitution of two more Fe atoms, forming a tetrahedral site [Fe^{3+}(IV)] plus two original pentacoordinated sites. A trimer can be formed with the substitution of two more Fe atoms. Thus a higher concentration of Fe may increase the chain length. At the same time, a choice of positions become possible. Either a linear or a kinked chain can develop.

According to Mössbauer spectroscopy, $SrTi_{0.2}Fe_{0.8}O_{3-\delta}$ spectra show a mixture of Fe^{3+}(VI), Fe^{3+}(V), and Fe^{3+}(IV). These data show that the structure has randomly distributed a small amount of monomers and a large amount of dimers and trimers; thus oxygen can jump either directly to the next unit cell (from *A* to *B*) in Fig. 11 or perform "detours" combining two site jumps (from *A* to *C* and then from *D* to *B*) resulting in the same final momentum transfer along (0 *k* 0) crystallographic plane. One can assume that local jumps exist for monomers as well, which could be detected by very high resolution quasielastic neutron scattering (QENS) experiments.

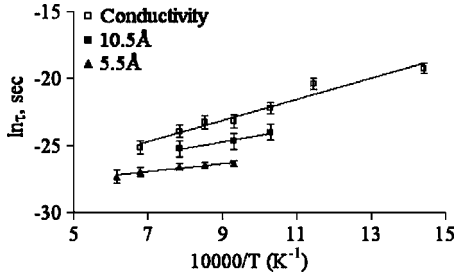

FIG. 12. Arrhenius plot of the characteristic dwell times measured at the time-of-flight spectrometer IN5 (10.5 and 5.5 Å) and by electrical conductivity.

From the linewidths of the two local motions observed by quasielastic neutron scattering, the characteristic jump times can be extracted and compared with data from electrical conductivity (Fig. 12). The Arrhenius plot visualizes again that two types of local motion assigned here to fast direct jumps (resolution for 5.5 Å) and to slow indirect jumps (resolution for 10.5 Å) are present. Both are distinctly different from the dynamics observed in electrical conductivity as demonstrated by significantly higher activation energy and by differing absolute values for the dwell times, which are much longer for the translational diffusion as compared to the values for the rotational motions.

ACKNOWLEDGMENTS

The authors would like to acknowledge C. McCammon for helpful discussions and for assistance in Mössbauer spectroscopy analysis. Funding was provided in part by the Deutsche Forschungsgemeinschaft (Germany) through Project No. MA 801/7-3.

[1] T. R. Clevenger, J. Am. Chem. Soc. **46**, 207 (1965).
[2] L. H. Brixner, Mater. Res. Bull. **3**, 299 (1968).
[3] J.-C. Grenier, M. Pouchard, and P. Hagenmuller, J. Solid State Chem. **58**, 243 (1985).
[4] Y. G. Wang, S. Steinsvik, R. Høier, and T. Norby, Mater. Lett. **14**, 1027 (1995).
[5] S. Steinsvik, R. Bugge, J. Gjønnes, J. Taftø, and T. Norby, J. Phys. Chem. Solids **58**, 969 (1997).
[6] J. Rodriguez, J. A. Pereda, M. Vallet, J. G. Calbert, and J. Tejada, Mater. Res. Bull. **21**, 255 (1986).
[7] S. Steinsvik, T. Norby, and P. Kofstad, Electroceramics 4.Verlag der Augustinus Buchhandlung **2**, 691 (1994).
[8] V. F. Sears, *Thermal-Neutron Scattering Length and Cross Sections for Condensed-Matter Research* (Theoretical Physics Branch, Chalk River Nuclear Laboratories, AECL-8490, 1984).
[9] R. Hempelman, *Quasielastic Neutron Scattering and Solid State Diffusion* (Oxford University Press, New York, 2000).
[10] M. Bee, *Quasielastic Neutron Scattering* (Adam Hilger, Bristol and Philadelphia, 1988).
[11] R. Scherm, Ann. Phys. (N.Y.) **7**, 349 (1972).
[12] C. T. Chudley and R. J. Elliot, Proc. Phys. Soc. London **77**, 353 (1961).
[13] J. D. Barns, J. Chem. Phys. **58**, 5193 (1973).
[14] A. J. Dianoux, F. Volino, and H. Hervet, Mol. Phys. **30**, 1181 (1975).
[15] A. J. Leadbetter and R. E. Lechner, in *The Plastically Crystalline State*, edited by J. N. Sherwood (Wiley, New York, 1975).
[16] F. Volino and A. J. Dianoux, Mol. Phys. **41**, 271 (1980).
[17] E. Siegel and K. A. Müller, Phys. Rev. B **19**, 109 (1979).
[18] W. Schmatz, Treatise on Material Science and Technology **2**, 105 (1975).
[19] P. H. Deterichs, J. Phys. F: Met. Phys. **3**, 471 (1973).
[20] G. S. Bauer, Treatise on Material Science and Technology **15**, 291 (1979).
[21] A. I. Becerro, F. Langenhorst, R. J. Angel, S. Marion, C. A. McCammon, and F. Seifert, Phys. Chem. Chem. Phys. **2**, 3933 (2000).
[22] A. I. Becerro, F. Seifert, R. J. Angel, S. Rios, and C. McCammon, J. Phys.: Condens. Matter **12**, 3661 (2000).
[23] C. McCammon, A. I. Becerro, F. Langenhorst, R. J. Angel, S. Marion, and F. Seifert, J. Phys.: Condens. Matter **12**, 2969 (2000).